Chinese Chemical Letters 36 (2025) 110277

Contents lists available at ScienceDirect

Chinese Chemical Letters

journal homepage: www.elsevier.com/locate/cclet

Hydrogen peroxide electrosynthesis *via* two-electron oxygen reduction: From pH effect to device engineering

Xuyun Lu, Yanan Chang, Shasha Wang, Xiaoxuan Li, Jianchun Bao, Ying Liu*

Jiangsu Collaborative Innovation Center of Biomedical Functional Materials, School of Chemistry and Materials Science, Nanjing Normal University, Nanjing 210023, China

ARTICLE INFO

Article history:
Received 10 December 2023
Revised 12 March 2024
Accepted 16 July 2024
Available online 16 July 2024

Keywords:
Electrocatalysis
Hydrogen peroxide
Oxygen reduction reaction
pH effect
Device engineering

ABSTRACT

As a versatile and environmentally benign oxidant, hydrogen peroxide (H_2O_2) is highly desired in sanitation, disinfection, environmental remediation, and the chemical industry. Compared with the conventional anthraquinone process, the electrosynthesis of H_2O_2 through the two-electron oxygen reduction reaction ($2e^-$ ORR) is an efficient, competitive, and promising avenue. Electrocatalysts and devices are two core factors in $2e^-$ ORR, but the design principles of catalysts for different pH conditions and the development trends of relevant synthesis devices remain unclear. To this end, this review adopts a multi-scale perspective to summarize recent advancements in the design principles, catalytic mechanisms, and application prospects of $2e^-$ ORR catalysts, with a particular focus on the influence of pH conditions, aiming at providing guidance for the selective design of advanced $2e^-$ ORR catalysts for highly-efficient H_2O_2 production. Moreover, in response to diverse on-site application demands, we elaborate on the evolution of H_2O_2 electrosynthesis devices, from rotating ring-disk electrodes and H-type cells to diverse flow-type cells. We elaborate on their characteristics and shortcomings, which can be beneficial for their further upgrades and customized applications. These insights may inspire the rational design of innovative catalysts and devices with high performance and wide serviceability for large-scale implementations.

1. Introduction

Owing to its strong oxidizing properties across a wide pH range ($E^0 = 1.763$ V at pH 0 and $E^0 = 0.878$ V at pH 14), hydrogen peroxide (H_2O_2) is extensively used in disinfection, bleaching, water treatment, and chemical synthesis [1-3]. The global market demand for H_2O_2 is projected to exceed $6.2 billion by 2026 [4]. Currently, industrial H_2O_2 is mainly synthesized by a multistep anthraquinone oxidation process, which accounts for >95% of total market production [5]. Nevertheless, this method consumes a substantial amount of energy and relies on costly palladium-based hydrogenation catalysts [6]. Additionally, practical applications require vacuum distillation and purification steps to achieve high H_2O_2 concentrations, resulting in additional expenses and safety concerns during storage and transportation [7,8]. Alternatively, H_2O_2 can be synthesized directly on a small scale using catalysts such as Pd, Pt, and other metals or alloys through the reaction of H_2 and O_2 [9,10]. However, the mixture of H_2 and O_2 poses explosion risks, limiting its widespread applications [11,12]. Moreover, the produced H_2O_2 still demands additional storage and transportation procedures for practical use. Photocatalytic H_2O_2 production on polymeric carbon nitrides is also a promising method for green H_2O_2 synthesis but is still limited by low activity and efficiency [13-17]. Actually, for most industries, on-site production and decentralized application of H_2O_2 are preferred [18]. Consequently, there is a growing interest in developing "on-demand" methods for H_2O_2 production and exploring benign operating conditions [19].

Electrochemical oxygen reduction reaction (ORR) through a $2e^-$ transfer process offers a sustainable and mild method for on-site H_2O_2 production from O_2 under ambient conditions [20-22]. However, when compared with the competitive $4e^-$ pathway ($O_2 + 4H^+ + 4e^- \rightarrow 2H_2O$, $E^0 = 1.23$ V *vs.* RHE), the $2e^-$ pathway of O_2 ($O_2 + 2H^+ + 2e^- \rightarrow H_2O_2$, $E^0 = 0.70$ V *vs.* RHE) demonstrates a more negative standard potential, making it thermodynamically less favorable. To this end, advanced catalysts with high selectivity for H_2O_2 electrosynthesis are highly desired [23]. To date, numerous catalysts have been investigated, including precious metals (*e.g.*, $PtHg_4$, PdAu) [24,25], carbon-based materials (*e.g.*, O-CNTs, N-FLG) [26,27], metal-organic frameworks (MOFs, *e.g.*, $Mg_3(HITP)_2$, Ni MOF NSs) [28,29], transition metal oxides (*e.g.*, ZnO, Ti_2O_3) [30,31], dichalcogenides (*e.g.*, $CoSe_2$, $Ni_2Mo_6S_8$) [32-34], and borides (*e.g.*, Ni_3B) [35]. Notably, these catalysts exhibit different reaction be-

* Corresponding author.
E-mail address: liuyingg@njnu.edu.cn (Y. Liu).

https://doi.org/10.1016/j.cclet.2024.110277
1001-8417/

haviors under different pH conditions. For instance, carbon-based materials excel in the selective reduction of O_2 to produce H_2O_2 in alkaline media but demonstrate limited electrocatalytic ability in acidic environments [36]. In contrast, precious metal-based materials still dominate in acidic conditions [37]. These disparities arise from variations in the reaction mechanisms under different pH conditions. Furthermore, the dissociation constant of H_2O_2 is 11.69 (pK_{a1}) at 25 °C [38], implying that H_2O_2 can exist as a molecule in acidic or neutral media, whereas in alkaline environments, it may undergo deprotonation to form HO_2^- [39]. Hence, the pH level of the electrolyte significantly influences H_2O_2 electrosynthesis. In terms of practical applications, different pH conditions cater to various fields. For example, alkaline media are suitable for textile and paper pulp bleaching applications. In comparison, H_2O_2 has a wider range of applications in acidic and neutral environments, such as electro-Fenton degradation of diverse pollutants in acidic conditions and bacteria killing, water disinfection, value-added chemical synthesis in neutral conditions [40-42]. Overall, electrochemical H_2O_2 production in different pH conditions is a complex, multifactorial process, and its application is a cross-disciplinary, flexible field.

Apart from catalyst engineering and the pH effect, the production capacity of H_2O_2 is another crucial factor for its industrial applications [43]. In laboratory research, rotating ring-disk electrode (RRDE) and H-type cell setups are initially adopted to evaluate the selectivity and yield of H_2O_2, respectively [44]. However, the low solubility of O_2 in the electrolyte and the limited diffusion of O_2 to the electrode surface hinder high current densities and continuous decentralized H_2O_2 production. To address this issue, flow-type cells (assembled with a gas-diffusion electrode (GDE)), dual-membrane flow cells (with a solid electrolyte (SE)), and membrane-free gas-liquid separated cells were subsequently proposed to meet the diverse requirements of industrialization. These requirements include direct use without purification, membrane-free reactors to reduce costs, and streamlined production processes [45-48].

Thus far, diverse catalysts and devices have been developed, and considerable progress has been achieved. However, the design principles and correlations of catalysts under different pH conditions have not been systematically studied. Moreover, the primary obstacle impeding the practical on-site application of H_2O_2 is still the insufficient capacity for H_2O_2 production. Therefore, more highly efficient and cost-effective catalysts and devices should be exploited to ameliorate these situations. Previous reviews have reported diverse two-electron ORR ($2e^-$ ORR) catalysts and relevant modulation strategies. For example, Zhang *et al.* introduced recent progress made in different types of metal-free carbon-based catalysts from the perspective of dimensions, including three-dimensional, two-dimensional, one-dimensional, and zero-dimensional [23]. Moreover, various strategies, including heteroatom doping, structural engineering, and defect engineering, are examined for their role in enhancing catalytic efficiency. Yang *et al.* summarized recent methodologies (including tuning metal center sites, engineering surface functionalization and coordination environments) and achievements of single-atom catalysts (SACs), particularly M-N-C catalysts, for the selective $2e^-$ ORR to produce H_2O_2 [18]. Combined with theoretical computation and characterization, they elucidate the synthesis–structure–property correlation and highlight the basic properties that impact activity and selectivity, followed by a perspective on the effective strategies to address the stability issue during H_2O_2 production. Differentially, this review focuses on the differences in catalytic mechanisms and design principles at different pH conditions, as well as the most salient features of the production devices. The aim is to provide insights into the design and synthesis of an effective $2e^-$ ORR electrocatalyst with high selectivity, activity and yield, and to promote the development and adoption of advanced devices for scaling up the utilization of H_2O_2 and customized applications. The content of this review can be divided into three parts, as shown in Fig. 1. First, using $2e^-$ ORR under different pH conditions as a clue, we survey and analyze recent advances in catalytic mechanisms, design principles, and the potential applications of relevant catalytic systems. Second, in response to diverse on-site application demands, we elaborate on the evolution of H_2O_2 electrosynthesis devices from laboratory scale to practical implementation, explaining their advantages and disadvantages, which are beneficial for their upgrading and customized application. Third, we propose the remaining challenges and future opportunities for achieving industrial-level H_2O_2 production. We hope this review will be helpful in guiding the design and discovery of innovative and efficient catalysts toward substantial H_2O_2 electrosynthesis.

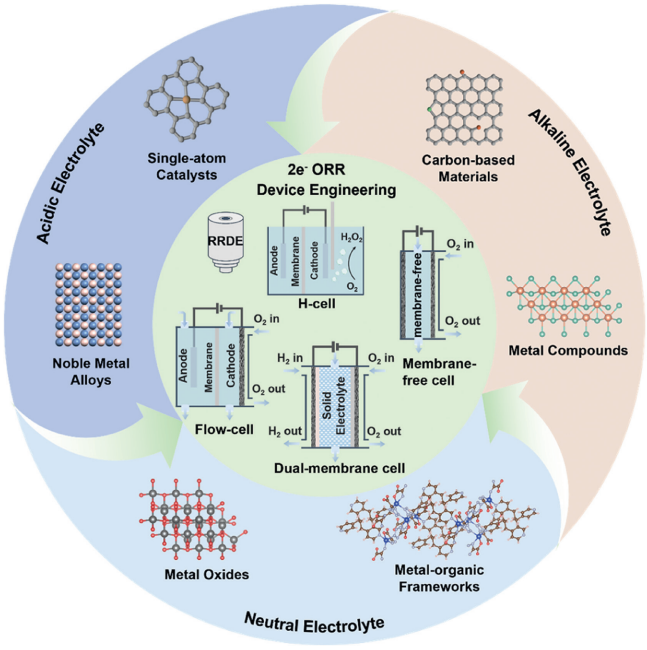

Fig. 1. Schematic diagram of catalytic mechanism and design principles for $2e^-$ ORR under different pH conditions and device engineering for H_2O_2 electrosynthesis.

2. Design principles and reaction mechanisms of catalysts under different pH conditions

2.1. In acidic electrolyte

2.1.1. Mechanism of acidic $2e^-$ ORR

Owing to the decent stability and diverse applications of H_2O_2 in acidic media, acidic H_2O_2 electrosynthesis holds great promise for industrial implementation. For instance, acidic H_2O_2 electrosynthesis can proceed directly in mature proton-exchange membrane (PEM) devices and electro-Fenton installations, which are valuable for chemical transformation and environmental treatment, respectively [49,50]. Its broad applicability has also facilitated the development of $2e^-$ ORR electrocatalysts, including noble metals and SACs, in acidic environments [51-54]. In principle, $2e^-$ ORR involves the transfer of two electrons (Fig. 2a) [55], and consists of a two-step proton-coupled electron transfer process in aqueous solutions at acidic pH, which can be represented by Eq. 1:

$$O_2 + 2H^+ + 2e^- \rightarrow H_2O_2,\ E^0 = 0.70\,V\ vs.\ RHE \quad (1)$$

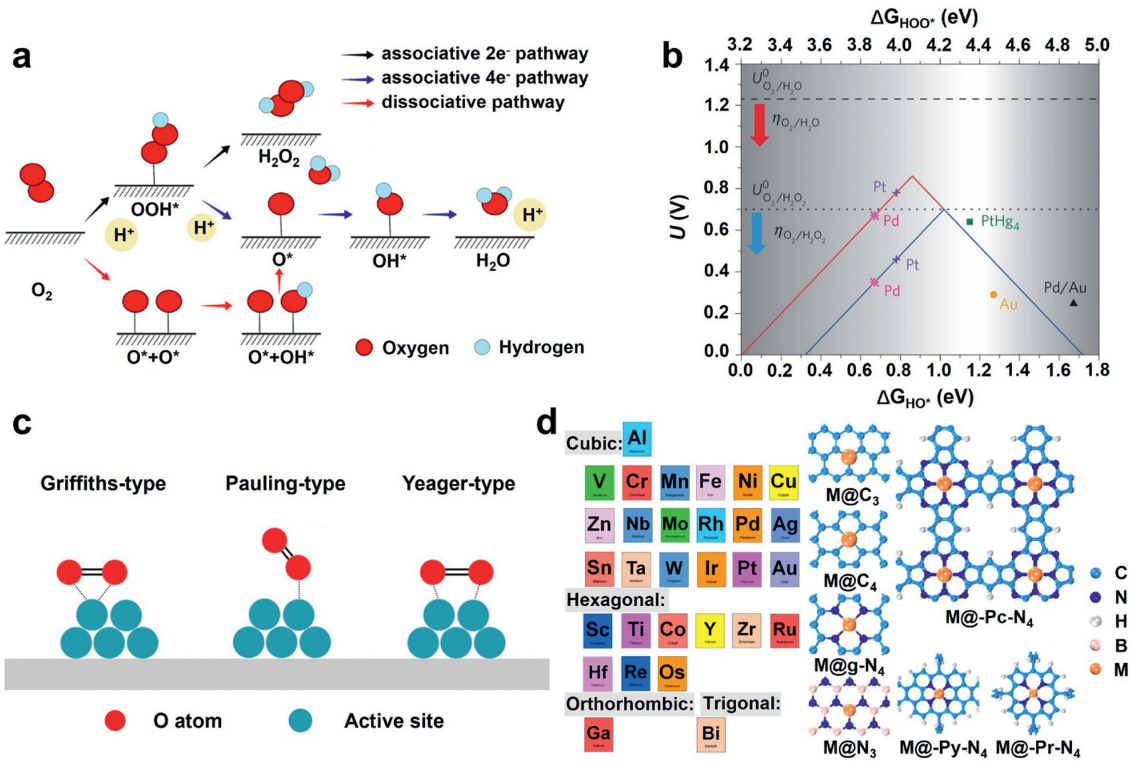

Fig. 2. (a) Pathway for 4e⁻ and 2e⁻ O_2 electroreduction. Reproduced with permission [55]. Copyright 2019, American Chemical Society. (b) Volcano plot for oxygen reduction to H_2O_2. The red solid line and blue solid line represent the theoretically calculated oxygen reduction volcano plot for the 4e⁻ and 2e⁻ ORR, with the limiting potential plotted as a function of ΔG_{HO*} (lower horizontal axis) and ΔG_{HOO*} (upper horizontal axis). In addition, η means the thermodynamic overpotential for a specific reaction. Reproduced with permission [24]. Copyright 2013, Springer Nature. (c) Possible configurations of O_2 adsorption on the catalyst surface. Reproduced with permission [7]. Copyright 2023, Springer Nature. (d) Screened metal atoms with their most stable bulk structures and a schematic illustration of all the considered SACs. Reproduced with permission [55]. Copyright 2019, American Chemical Society.

$$^* + O_2 + H^+ + e^- \rightarrow {}^*OOH \quad (1a)$$

$$^*OOH + H^+ + e^- \rightarrow H_2O_2 + ^* \quad (1b1)$$

$$^*OOH + H^+ + e^- \rightarrow {}^*O + H_2O \quad (1b2)$$

where * is the unoccupied surface binding site and *OOH is a critical intermediate. Eq. 1a represents the first step of proton-coupled electron transfer process to generate *OOH intermediate, and Eqs. 1b1 and 1b2 indicate that the generated *OOH undergoes a 2e⁻ pathway to produce H_2O_2 (associative 2e⁻ pathway) or a 4e⁻ pathway to produce H_2O (associative 4e⁻ pathway), respectively.

Alternatively, the initial O—O bond in the O_2 molecule may be directly broken (dissociative pathway), leading to the formation of two *O species (without the intermediate *OOH formation). These *O species can then gain protons and electrons to ultimately form H_2O. In the context of the 2e⁻ ORR and 4e⁻ ORR, key intermediates *OOH and *OH follow a linear scaling relationship (typically $\Delta G_{HOO*} = \Delta G_{HO*} + 3.2$ eV), resulting in the creation of 2e⁻ and 4e⁻ ORR volcano-type plots (Fig. 2b) [24]. As shown in Fig. 2b, it becomes evident that the 2e⁻ ORR activity is primarily determined by the adsorption energy of *OOH (ΔG_{HOO*}). The equilibrium potential of the volcano peak is 0.70 V, which corresponds to a catalyst with the optimal binding strength of *OOH intermediate. At the left segment of the volcano plot, the catalyst exhibits stronger binding to *OH and *OOH species, favoring the 4e⁻ reduction pathway to produce H_2O. At the right segment of the volcano plot, the catalyst has a weaker binding to *OOH, which tends to enhance selectivity but reduce activity in the formation of H_2O_2. Guided by this volcano plot, the catalyst situated at the apex is defined as the ideal material with the highest electrocatalytic activity for 2e⁻ ORR [56,57]. Furthermore, from this free energy diagram, we can discern the propensity of different catalysts to undergo the desired 2e⁻ or competing 4e⁻ reduction pathway, allowing us to screen the most promising candidates for selective H_2O_2 production. To achieve optimal ΔG_{HOO*}, the O_2 adsorption mode is a crucial consideration. Typically, there are three recognized ways for oxygen adsorption, *i.e.*, Griffiths-type, Yeager-type and Pauling-type (Fig. 2c) [7]. The 4e⁻ pathway is typically favored through a "side-on" adsorption of O_2, known as the Griffiths-type, where the O_2 molecule adsorbs side-on to a single metal atom. Another pathway, known as the Yeager-type, involves the bridge adsorption of the O_2 molecule on two adjacent metal atoms, also promoting a 4e⁻ reaction. This is primarily because both pathways involve the dissociation of the O-O bond. In contrast, the "end-on" adsorption of O_2, known as Pauling-type, prefers a 2e⁻ pathway to produce the desired H_2O_2.

2.1.2. Electrocatalysts for acidic H_2O_2 production

Over the past decades, platinum group metals (PGMs) have been intensively studied for their appropriate adsorption energy and mode for the 4e⁻ pathway, establishing them as state-of-the-art 4e⁻ ORR catalysts [58]. To maximize the 2e⁻ reaction route, it is essential to manipulate the local structure of PGMs and adjust the type of O_2 adsorption to the "end-on" mode. Accordingly, various strategies have been employed, including alloying with inert metals (*e.g.*, Hg, Ag, and Au) and incorporating nonmetal elements (including O, S, Se, and P) to tailor the accessibility of active sites [59-61]. For example, by using Au as the inert metal, Zhao *et al.* designed bimetallic PdAu nanoframes that exhibit remarkable H_2O_2

selectivity (>90%) and rapid electro-Fenton degradation rates for Rhodamine B within minutes [25]. Moreover, with Se as the non-metal element, Huang and co-workers fabricated amorphous $PdSe_2$ nanoparticles as highly selective catalysts for the electrochemical synthesis of H_2O_2 [62]. Density functional theory (DFT) calculations implied that the low-coordinated Pd sites could optimize the adsorption of oxygenated intermediates and maintain the integrity of the O–O bond, contributing to the high selectivity of 92%–98% at 0.0 – 0.3 V (*vs.* RHE).

Nevertheless, the essential high cost and scarcity of precious metals constrain their large-scale applications. Hence, researchers shifted their focus to SACs, which could offer ~100% utilization of metal atoms as active sites [63-66]. Although previous studies have reported a variety of SAC synthesis methods, more studies still remain on trial-and-error methods. To this end, Wang's group comprehensively summarized and compared the preparation methods of these trial-and-error synthesis strategies, including spatial confinement strategy, defect engineering strategy, coordination site design strategy, and atomic layer deposition strategy, putting forward some professional opinions, and aiming at guiding more rational and intelligent catalyst design and synthesis. Moreover, in light of the rapid development of SACs and the continuous expansion of application fields, they summarized the applications and research progress of SACs in different fields, such as environment catalysis, electrocatalysis, organic synthesis, photocatalysis, batteries, sensors, and enzyme catalysis. In addition, the design strategies and structure–activity relationships of SACs for specific reactions were summarized and analyzed, which are conducive to the personalized design and application of SACs [67,68].

Moreover, there is a significant difference between SACs and bulk metals, which can be understood through the interplay between the geometrical effect and the ligand/electronic effect. Essentially, according to Eq. 1b, to achieve high catalytic activity, the adsorption of *OOH should be enhanced. By contrast, to obtain high selectivity, the adsorption of *O (the product of *OOH dissociation) should be reduced. On a metal surface, *OOH and *O intermediates normally adsorb on atop sites and hollow sites, respectively. Conversely, for a SAC, only atop sites are available for adsorption due to the discontinuous and isolated atomic site. This characteristic helps SACs specifically stabilize the *OOH and destabilize *O intermediates, breaking the linear scaling relationship between ΔG_{HOO*} and ΔG_{HO*}. This allows for superior $2e^-$ ORR selectivity and activity to be achieved synchronously. Given this circumstance, a large number of SACs, such as CoNOC [69], Co_1–NG(O) [70], penta-coordinated O–Co–N_2C_2 [71], oxygen-rich MesoC–Co nanosheets [72], β-substituted CoPorF/CNT [73], CB@Co–N–C [74], CoIn–N–C [75], Ni–N_2O_2/C [76], and Mo_1/OSG-H [77], have been exploited, and remarkable $2e^-$ ORR selectivity and activity are realized.

Furthermore, by modifying SACs with different structural motifs, it may be possible to break the linear scaling relation and achieve more glorious electrocatalytic performances. For instance, Guo *et al.* constructed and screened 210 SAC models by rationally anchoring a series of single metal atoms on several representative and experimentally achievable substrates (Fig. 2d) [55]. It was elucidated that for SACs with metal atoms in groups 3 to 10, increasing the number of d-electrons of metal atoms tends to weaken the interaction between the metal atom active sites and *O, thereby improving the selectivity of H_2O_2 electrosynthesis. The host matrix and local coordination environment were found to dramatically modify the electronic structure and adsorption capability of the metal center in SACs, consequently altering the activity and selectivity of these catalysts. Notably, it was revealed that macrocyclic structures outperformed graphene- and BN-based materials in terms of overall performance. Collectively, microstructure and electrocatalytic performance are closely correlated, and by modifying the metal center, local coordination configuration, or host matrix of SACs, exceptional performances may be achievable.

2.2. In alkaline electrolyte

2.2.1. Mechanism of alkaline $2e^-$ ORR

In the 1930s, Berl *et al.* pioneered H_2O_2 electrosynthesis in alkaline media using activated carbon cathode *via* $2e^-$ ORR [78]. Since then, this technology, known as Huron–Dow process, has been continuously developed and successfully implemented in the production of dilute alkaline H_2O_2 solutions used for textile and paper pulp bleaching. Essentially, the reaction equation and electron pathways for $2e^-$ ORR in an alkaline solution are illustrated in Eq. 2:

$$O_2 + H_2O + 2e^- \rightarrow HO_2^- + OH^-,\ E^0 = 0.76\ \text{V}\ \textit{vs.}\ \text{RHE} \quad (2)$$

$$^* + O_2 + H_2O + e^- \rightarrow {}^*OOH + OH^- \quad (2a)$$

$$^*OOH + e^- \rightarrow HO_2^- + ^* \quad (2b)$$

here, * represents the catalyst surface site. The process starts with O_2 on the catalyst surface protonating to form *OOH, which then combines with an electron to form HO_2^-. Notably, that in alkaline media, H_2O_2 exists primarily as HO_2^-. The proper absorption and desorption of *OOH are crucial for facilitating the desorption of HO_2^-. Consequently, similar to acidic conditions, the selectivity of $2e^-$ ORR in alkaline environments is also contingent upon the adsorption energy of the *OOH intermediate. Furthermore, the preservation of the O-O bond on the catalyst surface site plays a decisive role in the selective H_2O_2 electrosynthesis under alkaline conditions.

2.2.2. Electrocatalysts for alkaline H_2O_2 production

To counter this situation, a series of catalysts have been studied, and diverse research strategies have been adopted to fine-tune the absorption and desorption balance of *OOH [79-81]. For example, carbon-based materials were initially considered due to their relatively weak interaction with *OOH, which promotes the desorption of HO_2^- and results in decent selectivity for H_2O_2 production [39,82]. Nevertheless, they still faced a hurdle in terms of a high O_2 adsorption barrier. Modification methods, including oxygen functionalization, defect engineering and heteroatom doping of carbon-based materials, are emphasized in Supporting information (see the modification methods of carbon-based materials and Fig. S1 for details).

Aside from carbon-based materials, other materials such as metal oxides [83,84], dichalcogenides [34,85], and borides [35,86], have also demonstrated attractive electrocatalytic behaviors under alkaline conditions. By comparison, it was noticed that under different pH conditions, different types of catalysts are preferred for H_2O_2 production. For instance, Yang *et al.* observed that glassy carbon (GC) showed both high activity and selectivity in alkaline conditions, but its activity was limited in acidic environments (Fig. 3a) [44]. The Pourbaix diagram, which depicts the thermodynamically stable state of the catalyst surface as a function of pH and electrode potential in an electrochemical system, may provide an explanation for this phenomenon. Specifically, when using metal-free carbon as a catalyst, it has been demonstrated that catalyst configurations with higher oxygen content exhibit greater stability under high pH and potential conditions, whereas configurations with higher hydrogen are more stable under low pH and potential conditions (Fig. 3b) [87]. Hence, catalysts with oxygen-related groups usually tend to exhibit superior electrocatalytic performance in alkaline and neutral electrolytes [88].

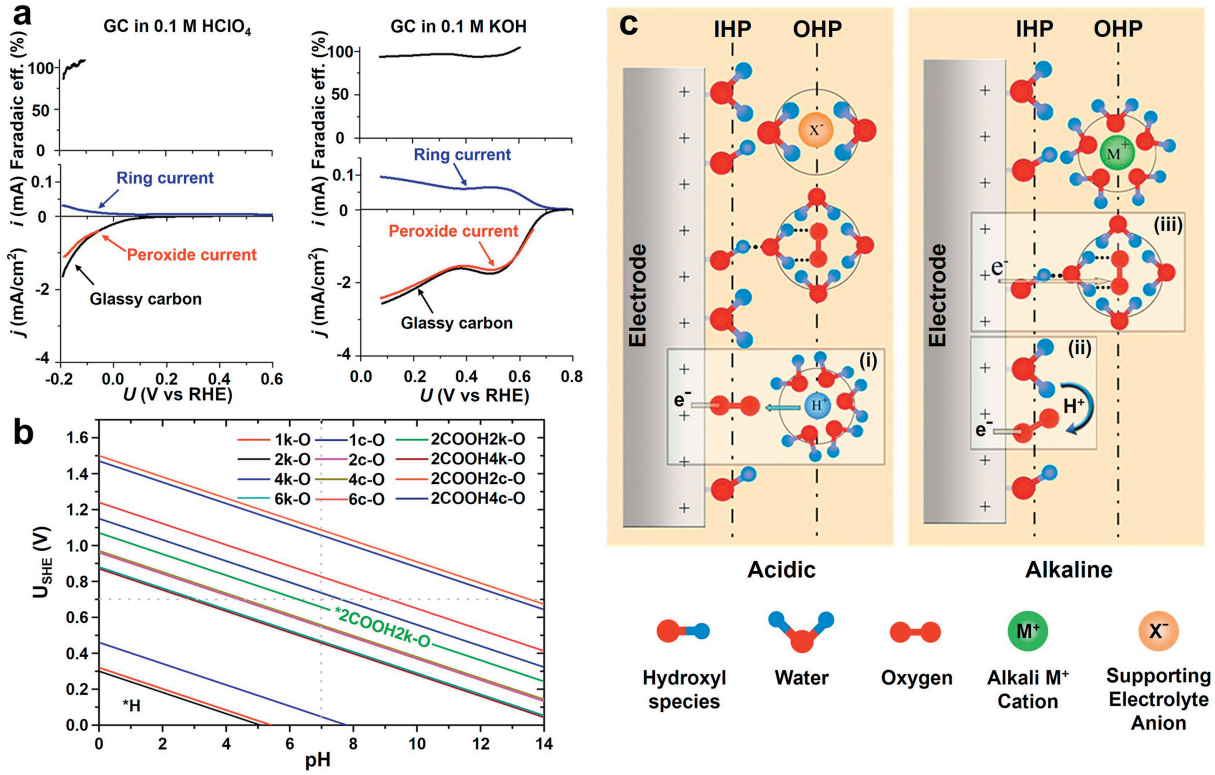

Fig. 3. (a) ORR of GC in 0.1 mol/L $HClO_4$ and 0.1 mol/L KOH. Reproduced with permission [44]. Copyright 2018, American Chemical Society. (b) Pourbaix diagram showing the most energetically favorable surface species configurations as a function of reaction conditions of electrode potential and pH. The k-O, c-O and COOH represent the ketone oxygen, CO group, and COOH group, respectively. The digits before k-O, c-O and COOH represent the amount of corresponding oxygen configurations doped into the carbon substrate in relevant structural models. A larger digit represents more oxygen configurations, and less hydrogen content. Reproduced with permission [87]. Copyright 2020, American Chemical Society. (c) Schematic illustration of the double-layer structure during ORR in acidic (left) and alkaline (right) conditions. Insets (i) and (ii) represent the inner sphere pathway in acidic and alkaline conditions, respectively, while inset (iii) represents the outer sphere pathway in an alkaline condition. Reproduced with permission [89]. Copyright 2011, American Chemical Society.

In addition to considering the stability of the functional groups under reaction conditions, it is crucial to examine the electron transfer mechanisms that occur under different pH conditions, as these mechanisms can significantly impact the activity of metal-based catalysts. Ramaswamy *et al.* investigated the effect of traversed pH conditions (from acidic to alkaline media) on the adsorption behavior of reactants, intermediates, and products. They discovered that changes in pH led to variations in adsorption strength and the location of species adsorption within the double-layer structure (Fig. 3c) [89]. Specifically, two mechanisms, namely, the inner sphere electron transfer process and the outer sphere electron transfer process, have been proposed in relation to the ORR process. The inner-Helmholtz plane (IHP) is composed of adsorbed hydroxyl species, chemisorbed O_2, and solvent water dipoles. By contrast, the outer-Helmholtz plane (OHP) contains solvated alkali metal ions and solvated O_2 cluster $O_2{\cdot}(H_2O)_n$ in alkaline media. In the case of a typical inner-sphere electron transfer process, the electrons are first transferred to $O_{2,ads}$ to form superoxide $(O_2^{\bullet-})_{ads}$. Subsequently, the $(O_2^{\bullet-})_{ads}$ intermediates are protonated by direct proton transfer (in the acidic condition, inset (i) process) or indirect proton transfer from water molecules (in the alkaline condition, inset (ii) process). However, elevated pH under alkaline conditions causes a decrease in the rate of water activation, making the proton transfer process more challenging to proceed. Therefore, an outer-sphere electron transfer process is proposed in alkaline media (inset (iii) process). For an outer-sphere electron transfer process, the electron transfer process occurring in the outer sphere enables the noncovalent interaction between the solvated O_2 cluster and the OH_{ads} adsorbed on electrode surface. This interaction leads to the formation of HO_2^- anion, followed by electrostatic repulsion between the adsorbed OH_{ads} and HO_2^-, resulting in the desorption of HO_2^- anion into the electrolyte. Under the circumstances, the nonspecific adsorption of OH_{ads} on the surface of nonnoble metals and metal oxides enables them to be promising candidates for $2e^-$ ORR under alkaline conditions. Importantly, in alkaline media, the potential of the working electrode decreases compared with acidic conditions, resulting in excess charge on the electrode surface. This excess charge favors the existence of HO_2^- intermediate, thereby contributing to superior $2e^-$ ORR activity.

2.3. In neutral electrolyte

Electrocatalysts for neutral H_2O_2 production: Compared with acidic and alkaline conditions, the neutral solution is noncorrosive. This is particularly advantageous for the direct production and application of pure H_2O_2 without the need for further neutralization procedures. For instance, the generated H_2O_2 can be used directly in rainwater treatment and organic synthesis [90,91]. The reaction mechanism in neutral electrolytes is similar to that in acidic electrolytes, so here we focus on the progress of $2e^-$ ORR electrocatalysts, with a particular emphasis on some unusual examples. As described in Section 2.1, isolated active sites can facilitate the selective formation of H_2O_2. Therefore, researchers have explored noble metal catalysts with discontinuous active sites first. To improve the isolation of noble metal atoms, Li *et al.* introduced phosphorus (P) elements and prepared PtP_2 nanocrystals (NCs) [92]. Thanks to the optimized adsorption of the key intermediate *OOH, the PtP_2 NCs, functioning as cathodic catalysts, played an important role in the neutral polymer electrolyte membrane fuel cell (PEMFC),

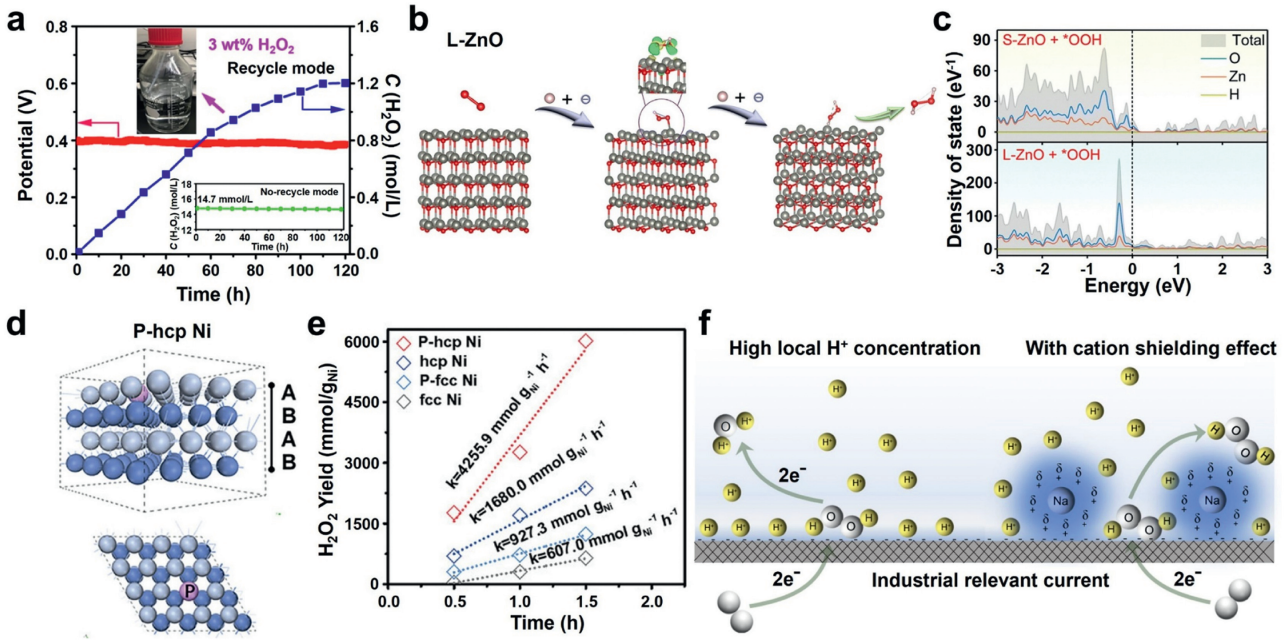

Fig. 4. (a) Time-dependent neutral H_2O_2 concentration measured at a constant potential of 0.4 V (*vs.* RHE) for 120 h. The accumulated H_2O_2 concentration was continuously cycled through the system (600 mL). Reproduced with permission [92]. Copyright 2020, Springer Nature. (b) Illustration of the 2e⁻ ORR to H_2O_2 over L-ZnO. (c) DOS of S- and L-ZnO absorbed *OOH. Reproduced with permission [30]. Copyright 2023, Royal Society of Chemistry. (d) Schematic structures of metastable P-hcp Ni. The different blue balls are Ni in different layers and the pink ball is P. (e) H_2O_2 yields of different catalysts in 1.0 mol/L Na_2SO_4 by using the flow cell device. Reproduced with permission [99]. Copyright 2023, Wiley–VCH. (f) Schematic illustration of 2e⁻ ORR toward H_2O_2 in acid electrolyte with or without Na^+ under industrial-relevant current. Reproduced with permission [102]. Copyright 2022, Springer Nature.

achieving a high H_2O_2 production rate of 2.26 mmol h^{-1} cm^{-2} and long-term stability lasting up to 120 h at a high current density of 150 mA/cm^2 (Fig. 4a).

In recent years, there has been a growing interest in metal compounds as alternative catalysts to the extensively studied noble metal and carbon-based catalysts for 2e⁻ ORR [28,93-96]. To enhance the 2e⁻ ORR activity of these metal compounds, tremendous efforts have been dedicated to tailoring their geometric and phase structures. From a geometrical perspective, the reduction in size from microscale to nanoscale and, eventually, to the cluster/single-atom level can increase the exposure of catalytic sites, thereby boosting H_2O_2 production activity [97,98]. Interestingly, an abnormal size effect in ZnO nanoplates was observed by Chen's group [30]. As depicted in Figs. 4b and c, theoretical calculations and *in situ* Raman spectra revealed that, compared with small-thickness ZnO (S-ZnO), the d-band of large-thickness ZnO (L-ZnO) shifted toward the Fermi level. The shift stabilized the crucial reaction intermediate, ultimately resulting in ~100% selectivity and achieving ampere-level current density (1 A/cm^2). In addition to the geometric effect, phase transformation has proven effective in enhancing the intrinsic activity of active sites. As shown in Figs. 4d and e, Geng *et al.* prepared a phosphorus-optimized metastable hexagonal-close-packed phase nickel catalyst (P-hcp Ni) [99]. This catalyst utilized P atoms as stabilizers for the metastable hcp phase while also attracting electrons from the surrounding Ni to weaken the adsorption of *OOH and contribute to a remarkable H_2O_2 productivity of 4255.9 mmol g_{Ni}^{-1} h^{-1} in a neutral electrolyte in a flow cell. Analogously, Kang and co-workers reported a metastable hexagonal SnO_2 (h-SnO_2) nanoribbon with a space group of *P63/mmc* (194) [100]. DFT analyses showed that the h-SnO_2 (1−210) surface, primarily the side face of the nanoribbons, had an appropriate adsorption energy for *OOH. Thus, the h-SnO_2 electrocatalysts could trigger H_2O_2 synthesis in 0.1 mol/L Na_2SO_4 with a high selectivity of 99.99% and yield of 3885.26 mmol g^{-1} h^{-1} at 0 V (*vs.* RHE).

Notably, due to the continued consumption of protons during the ORR process, there is an alkaline shift in the local pH value of the electrode surface. Interestingly, Gyenge *et al.* discovered that the elevation in the local pH level could significantly improve the relevant current efficiency, increasing it from 12% to 61% in alkaline electrolyte and from 14% to 55% in acidic electrolyte [101]. Specifically, by using trialkylmethylammonium chloride (A336) as a cationic surfactant to displace protons in the electric double layer, theoretical estimations have indicated that the pH of the electrode surface can increase from 0.9 to a range of 2.0–9.4. These results indicate that by modulating the protons on the electrode surface, significantly enhanced electrocatalytic performance may be achieved. Correspondingly, Zhang *et al.* employed a cation-regulated interfacial engineering approach to augment 2e⁻ ORR, achieving an industrial-level rate under acidic conditions [102]. Molecular dynamic simulations have shown that in the presence of alkali metal cations, a "shielding effect" occurs, which dilutes the protons at the catalyst/electrolyte interface, thereby inhibiting the electrochemical dissociation of H_2O_2 to H_2O (Fig. 4f). Of course, if strictly neutral conditions are required, a buffer electrolyte solution is essential for evaluating 2e⁻ ORR at a neutral pH value, as proposed by Jin and Schmidt *et al.* [93]. Overall, understanding the local proton concentration and pH change at the electrode/electrolyte interface can provide valuable insights into molecular and mesoscopic engineering approaches for more efficient 2e⁻ ORR catalysis.

3. Device engineering for H_2O_2 bulk generation and utilization

In addition to the research on the development of robust electrocatalysts, there is an equally relevant pursuit of engineering proper electrochemical devices for on-site bulk generation of H_2O_2, since the "real-scenario" production of H_2O_2 is more conducive to versatile applications. In laboratory research, the RRDE setup is usually adopted for the expeditious evaluation of potential cata-

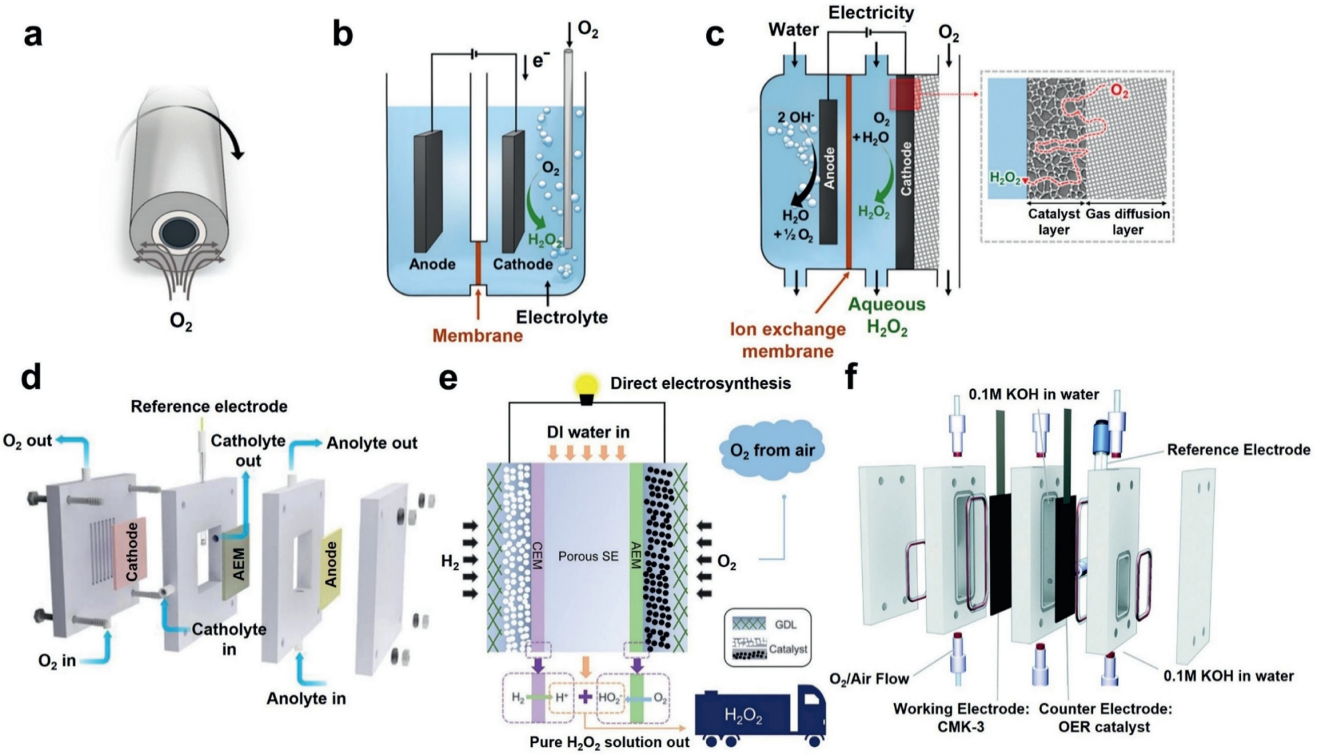

Fig. 5. Schematics for (a) a RRDE, (b) an H-cell configuration with a catalyst deposited on a solid substrate in a nonflowing electrolyte and (c) a continuous flow cell with a catalyst deposited on a GDE. Reproduced with permission [103]. Copyright 2020, American Chemical Society. (d) Schematic diagram of a GDE used for H_2O_2 electrosynthesis. Reproduced with permission [86]. Copyright 2022, Wiley–VCH. (e) Dual-membrane cell with pure H_2 and O_2 streams separately introduced to the anode and cathode, respectively. Reproduced with permission [91]. Copyright 2019, Springer Nature. (f) Membrane-free cell consisting of a flow channel. Reproduced with permission [114]. Copyright 2017, Royal Society of Chemistry.

lysts (Figs. 5a and b) [103]. Typically, with continued stirring, oxygen is transported to the GC disk electrode to occur in $2e^-$ and $4e^-$ ORR. Subsequently, the produced H_2O_2 is detected and quantified at the concentric platinum ring electrode. The applied potential for this process is set at $1.2-1.3$ V (*vs.* RHE) [104]. For bulk production and storage of H_2O_2, it is conducted in an H-type cell, which features two distinct electrolyte chambers. The accumulated H_2O_2 can be quantified using the potassium permanganate ($KMnO_4$)-based titration method, the ceric sulfate ($Ce(SO_4)_2$)-based ultraviolet-visible (UV–vis) spectroscopy method, or the potassium titanium(IV) oxalate ($K_2TiO(C_2O_4)_2$)-based UV–vis spectroscopy method. In the $KMnO_4$ assay, the MnO_4^- anion can be reduced to Mn^{2+} by H_2O_2 ($2MnO_4^- + 5H_2O_2 + 6H^+ \rightarrow 2Mn^{2+} + 8H_2O + 5O_2$), resulting in a change in solution color from dark purple to colorless. In contrast, the ($Ce(SO_4)_2$)-based UV–vis spectroscopy method may provide more accurate results owing to the stable reaction between $Ce(SO_4)_2$ and H_2O_2 ($2Ce^{4+}$ (yellow) $+ H_2O_2 \rightarrow 2Ce^{3+}$ (colorless) $+ 2H^+ + O_2$). In this approach, H_2O_2 concentration is quantitatively measured by comparing the absorbance of Ce^{4+} at a wavelength of 320 nm based on their linear correlation relationship. For the potassium titanium(IV) oxalate method, colorless titanium(IV) is oxidized by H_2O_2 to an orange titanium(IV)-peroxide complex in the presence of sulfuric acid. Subsequently, the concentration of H_2O_2 can be measured at a wavelength of 400 nm [105,106].

However, the low solubility of O_2 in the electrolyte and the limited diffusion of O_2 to the surface of submerged electrodes hinder the high current density and continuous decentralized H_2O_2 production [107]. To address these limitations, GDE (assembled in flow-type cells) was developed as an alternative electrode. As shown in Fig. 5c, the GDE consists of a porous layer containing a hydrophobic component, and the catalyst is deposited onto the GDE at the solid-liquid interface. This enables the direct delivery of oxygen to the catalyst surface without being restricted by the gas transport limitation [108,109]. During electrocatalysis, the generated H_2O_2 product is directly dissolved in the flowing electrolyte and steadily circulated within the electrode compartment. This reduces the concentration of H_2O_2 on the electrode surface, prevents the accumulation or decomposition of H_2O_2, and increases the total concentration of H_2O_2 in the electrolyte, resulting in a high concentration of H_2O_2 solution. For instance, in a recent study, Wu *et al.* reported a GDE coated with amorphous NiB_2 [86], and the assembled flow cell achieved a high H_2O_2 yield of 4.753 mol g^{-1} h^{-1} and long-term operation stability of 12 h at 125 mA/cm^2 (Fig. 5d). Analogously, Zhang *et al.* operated a natural air diffusion electrode and reached a high H_2O_2 rate of 6.72 mol $g^{-1}_{catalyst}$ h^{-1} in neutral solution [110]. The above devices are all based on GDEs. In addition to the GDE, Zhou *et al.* have reported an innovative "floating" electrode, in which one side of the electrode is open to the air and the other side is submerged in the aqueous solution [111]. This special approach enables the formation of a three-phase boundary (gaseous O_2, aqueous electrolyte, and solid cathode), thus allowing synergistic utilization of O_2 from both ambient air and the electrolyte. Thus, a high H_2O_2 yield of 61.7 mg/dm^3 was obtained using the "floating" electrode, which is 4.3 times higher than a conventional "submerged" cathode. Additionally, An *et al.* have proposed an anti-flooding air-breathing cathode (ABC, the anti-flooding herein refers to the prevention of catalyst flooding), which was prepared by a simple rolling-spraying method [112]. Then this ABC was amplified and integrated with the Ti/IrO_2-based anode to form a modular electrode system. In a 2 L prepilot scale system, the modular electrode could produce 322 ± 15.6 mg L^{-1} h^{-1} H_2O_2 with a current efficiency of 84.7%. Nevertheless, the H_2O_2 produced using this method is dissolved in the

electrolyte and may still require additional purification steps for certain specific applications.

To address this issue, Xia *et al.* reported on a two-type membrane flow cell that incorporated SE layers for the production of pure H_2O_2 solution [91]. As depicted in Fig. 5e, a porous SE layer was positioned between the cation and anion exchange membrane layers. This configuration facilitated ionic recombination, allowing H^+ and HO_2^- ions to cross from the anode and cathode, respectively, resulting in the direct production of H_2O_2. Subsequently, flushing the SE layer with deionized water produced a pure H_2O_2 aqueous solution. With this device, it could achieve a high H_2O_2 selectivity of >90% at 200 mA/cm^2 and a decent yield of 3.4 mmol cm^{-2} h^{-1} during continuous operation lasting up to 100 h. Additionally, Wei's group investigated the feasibility of this two-type membrane flow cell in coupling with organic oxidation [113]. In their experiment, the SE layer was mixed with an organic catalyst, titanium silicalite-1 (TS-1), and the generated H_2O_2 was captured by TS-1 to form Ti-OOH, an intermediate species with high oxidation activity. Ultimately, the organic compound underwent selective oxidization to obtain the desired value-added product.

While employing the two-type membrane SE approach can significantly reduce product crossover and avoid energy-intensive separation processes, the introduction of additional membranes leads to increased internal resistance within the device, thereby reducing production efficiency. Moreover, the polymer electrolyte membrane is susceptible to degradation by free radicals due to the self-decomposition of H_2O_2. In response to this question, Chen *et al.* adopted a membrane-free gas–liquid separated device in which a flowing electrolyte is placed between the cathode and anode [114]. The cathode, featuring a hydrophobic polymer on the backside, was coated with mesoporous carbon (CMK-3) capable of reacting with O_2 flow (Fig. 5f). Subsequently, the produced H_2O_2 was captured by the flowing electrolytes within the chamber. Analogously, Wang's group also reported a membrane-free H_2O_2 electrosynthesis flow cell [115]. Utilizing oxidized carbon nanotube and polytetrafluoroethylene polymer-decorated carbon fiber paper as the cathode and anode catalysts, respectively, this cell delivered a high cell efficiency of 153% and a large current of 50.4 mA at a cell potential of 1.7 V. This is mainly because the membrane-free cell allows for a decrease in cell voltage and overall ohmic loss, thereby opening up opportunities for practical applications [116].

Overall, in the above-mentioned cells, the early H-type cell is difficult to meet the industrial requirements for H_2O_2 production due to the low solubility of O_2/air in an aqueous solution. In recent years, with the development of flow-type cells and the rational use of the key component GDE, the mass transfer rate of gaseous reactants has significantly improved. Meanwhile, by adjusting the reaction area of the flow cell, the shape of the gas flow channel, and the gas/electrolyte flow rate, the 2e$^-$ ORR efficiency has also been significantly improved. Thus, the current density for H_2O_2 production was increased from tens of milliamps (mA) to amperes (A), thus realizing a significant breakthrough in H_2O_2 production performance. For example, Lin *et al.* reported a CoN_4/VG catalyst containing cobalt single atoms on vertically aligned graphene nanosheet assemblies [117]. It delivered a H_2O_2 productivity of 706 mmol $g_{catalyst}^{-1}$ h^{-1} in an H-cell setup, whereas in a gas-diffusion flow reactor, the associated productivity was considerably increased to 4000 mmol $g_{catalyst}^{-1}$ h^{-1}, confirming the high efficiency of the flow cell. Similarly, Zhang and colleagues prepared a carbon-supported Ni^{II} single-atom catalyst with $Ni-N_2O_2$ tetra-coordination ($Ni-N_2O_2$/C), which could be stabilized in a flow cell for 15 h at 70 mA/cm^2, far exceeding the behavior in an H-cell (8 h at 1 mA/cm^2) [76]. However, these new cells also present challenges in terms of device complexity and cost. Take the dual-membrane solid-electrolyte cell as an example; the GDEs (gas diffusion and catalyst layers), membranes (anion-exchange membrane and cation-exchange membrane), and solid polymer proton conductors are tightly compressed within a flow field plate [91,113]. Although the desired concentration of H_2O_2 can be obtained by setting parameters such as external gas input, liquid circulation, and operating temperature, the complexity of the components and parameterization makes operation and maintenance considerably more difficult. From this point of view, membrane-free cells can simplify operating conditions and reduce costs, and have been adopted in ethanol oxidation [118] and water splitting [119]. In addition, the membrane-free system can regulate the fluid in a laminar flow state with a low Reynolds number to prioritize convective transport over diffusive transport, thus avoiding oxidation of the as-prepared H_2O_2 on the anode [120]. Furthermore, compressing the individual membrane-free cells together to form a stack can further increase H_2O_2 productivity and reduce operating costs.

4. Conclusions and outlooks

In this review, we summarized recent advances in electrocatalysts and electrocatalytic devices for the 2e$^-$ ORR to produce H_2O_2, aspects of catalytic mechanisms in variable pH conditions, strategies for the rational design of electrocatalysts, and practical device engineering for scaling up H_2O_2 generation. We anticipate that the proposed mechanisms and insights may aid in the design and development of innovative catalysts and devices, thereby promoting large-scale H_2O_2 manufacturing. Overall, pH control plays an essential role in H_2O_2 production in different application environments. For example, alkaline H_2O_2 solutions can be used for textile and paper pulp bleaching, and the corresponding technology can be extended to anion-exchange membrane fuel cells to enable in-situ production of H_2O_2 while generating electrical energy. Therefore, the alkaline 2e$^-$ ORR catalytic system has been extensively investigated in previous reports. In acidic media, H_2O_2 has powerful oxidizing ability and wide applicability. Correspondingly, acidic H_2O_2 electrosynthesis can in turn be conducted in Fenton installations and mature PEM devices for environmental treatment and chemical transformation, respectively, with great application prospects. In neutral conditions, H_2O_2 can be used in the green organic synthesis of value-added chemicals, including epoxidation of alkenes, alcohol or thioether selective oxidation, and phenol hydroxylation. As for the design strategy of catalysts under different pH conditions, the proton concentration or degree of water activation, the adsorption strength of O_2, and the existence of H_2O_2 (the H_2O_2 molecule or HO_2^- anion) all have significant effects. Specifically, under acidic and neutral conditions, separated active sites are preferred to achieve the end-on adsorption mode of O_2, thereby promoting a 2e$^-$ ORR pathway. Moreover, the adsorption energy of the *OOH intermediate should be optimized to accelerate the desorption of H_2O_2. While in alkaline media, the outer-sphere transfer process should be considered first owing to the abundant adsorbed OH^- on the catalyst surface. To this end, non-precious metals and their oxides have become attractive alternatives for 2e$^-$ ORR. Despite significant progress and the development of diverse electrocatalysts and devices (Table S1 in Supporting information), several challenges remain related to H_2O_2 selectivity, activity, yield, and stability under different pH conditions, as well as practical and on-site applications.

First, a promising catalyst should exhibit high catalytic ability, applicability, low cost, and environmental friendliness. Currently, the reported 2e$^-$ ORR catalysts are primarily focused on carbon-based materials and metal oxides in alkaline electrolytes, whereas the alkali-catalyzed decomposition of H_2O_2 limits their widespread applications. Therefore, more attention should be shifted toward the development of 2e$^-$ ORR catalysts in acidic and neutral solutions to promote in-situ and stable applications of H_2O_2. Electro-

Fenton degradation is an emerging application of H_2O_2 in acidic conditions, where H_2O_2 can combine with Fe^{2+} to generate hydroxyl radicals (·OH) with strong oxidizing capacity for subsequent environmental treatment applications [93,121]. Additionally, the green organic synthesis of value-added chemicals is an essential application of H_2O_2 in neutral media [122-124]. Moreover, apart from the modulation strategies mentioned in this review, pore structure, hybrid/heterogeneous configuration, and hydrophilic/hydrophobicity have significant effects on H_2O_2 electrosynthesis. Therefore, it is necessary to select the appropriate catalyst type and modulation strategy comprehensively, obeying the reaction mechanisms and characteristics under different pH conditions, to achieve flexible regulation and customized applications.

Second, due to the pH- and catalyst type-dependent electrocatalytic properties of catalysts, along with complex operating conditions, it remains challenging to explore pH-universal $2e^-$ ORR catalysts and elucidate an explicit catalytic mechanism under tunable pH conditions. Confronted with this situation, first-principles theory and crucial characterization technologies (*e.g.*, synchrotron radiation, operando Raman spectroscopy, operando attenuated total reflectance infrared spectroscopy, and machine learning) may allow us to delve deeper into the adsorption and desorption behaviours of intermediates on catalyst surfaces under operating conditions and to identify the real active sites. This will help us gain a thorough understanding of the pH-dependent $2e^-$ ORR performances and facilitate the development of decentralized H_2O_2 synthesis, as well as its subsequent applications in chemistry, energy, and the environment fields.

Finally, the focus of H_2O_2 electrosynthesis should be on device engineering and the efficiency and durability of practical on-site applications. This can refer to well-established mature reaction systems and architectures, such as flow-type devices with GDEs and H_2-O_2 fuel cells. To achieve industrial-scale H_2O_2 yields, a porous, three-dimensional electrode (decorated with catalysts of appropriate thickness) is required to allow O_2 gas transport. Fluid flow systems are also needed to rinse away the generated H_2O_2 from the electrode surface for in-situ or next-step reactions. Additionally, the anodic half-reaction can be paired with other reactions (*e.g.*, alcohol oxidation, urea oxidation, and furfural oxidation) to construct an overall electrocatalytic platform, enabling the production of high−value chemical products and maximizing energy conversion efficiency.

Declaration of competing interest

The authors declare that they have no known competing financial interests or personal relationships that could have appeared to influence the work reported in this paper.

CRediT authorship contribution statement

Xuyun Lu: Conceptualization, Data curation, Investigation, Writing – original draft. **Yanan Chang:** Data curation, Investigation. **Shasha Wang:** Validation. **Xiaoxuan Li:** Validation. **Jianchun Bao:** Funding acquisition, Project administration, Supervision. **Ying Liu:** Conceptualization, Funding acquisition, Project administration, Supervision, Writing – review & editing.

Acknowledgment

This work was supported by the National Natural Science Foundation of China (Nos. 22102073, 22075147).

Supplementary materials

Supplementary material associated with this article can be found, in the online version, at doi:10.1016/j.cclet.2024.110277.

References

[1] J. Tang, T. Zhao, D. Solanki, et al., Joule 5 (2021) 1432–1461.
[2] J. Xie, L. Zhong, X. Yang, et al., Chin. Chem. Lett. 35 (2024) 108472.
[3] J.M. Campos-Martin, G. Blanco-Brieva, J.L.G. Fierro, Angew. Chem. 118 (2006) 7116–7139.
[4] H.W. Kim, M.B. Ross, N. Kornienko, et al., Nat. Catal. 1 (2018) 282–290.
[5] J.M. Campos-Martin, G. Blanco-Brieva, J.L. Fierro, Angew. Chem. Int. Ed. 45 (2006) 6962–6984.
[6] S.C. Perry, D. Pangotra, L. Vieira, et al., Nat. Rev. Chem. 3 (2019) 442–458.
[7] Y. Tian, D. Deng, L. Xu, et al., Nano-Micro Lett. 15 (2023) 122.
[8] A. Byeon, W.C. Yun, J.M. Kim, J.W. Lee, Chem. Eng. J. 456 (2023) 141042.
[9] Y. Bu, Y. Wang, G.F. Han, et al., Adv. Mater. 33 (2021) 2103266.
[10] R. Ciriminna, L. Albanese, F. Meneguzzo, M. Pagliaro, ChemSusChem 9 (2016) 3374–3381.
[11] K. Jiang, J. Zhao, H. Wang, Adv. Funct. Mater. 30 (2020) 2003321.
[12] Y. Wang, G.I.N. Waterhouse, L. Shang, T. Zhang, Adv. Energy Mater. 11 (2020) 2003323.
[13] J. Ma, X. Peng, Z. Zhou, Y. Shen, Y. Zhang, Chin. Chem. Lett. 34 (2023) 108784.
[14] H. Tan, P. Zhou, M. Liu, et al., Nat. Synth. 2 (2023) 557–563.
[15] Z. Teng, Q. Zhang, H. Yang, et al., Nat. Catal. 4 (2021) 374–384.
[16] J. Ma, X. Peng, Z. Zhou, et al., Angew. Chem. Int. Ed. 61 (2022) e202210856.
[17] J. Ma, C. Peng, X. Peng, et al., J. Am. Chem. Soc. 146 (2024) 21147–21159.
[18] X. Yang, Y. Zeng, W. Alnoush, et al., Adv. Mater. 34 (2022) 2107954.
[19] Y. Wen, T. Zhang, J. Wang, et al., Angew. Chem. Int. Ed. 61 (2022) e202205972.
[20] Z. Zhou, Y. Kong, H. Tan, et al., Adv. Mater. 34 (2022) 2106541.
[21] Y. Zhou, G. Chen, J. Zhang, J. Mater. Chem. A 8 (2020) 20849–20869.
[22] D. Ouyang, D. Gao, J. Hong, Z. Jiang, X. Zhao, J. Energy Chem. 79 (2023) 135–147.
[23] D. Zhang, E. Mitchell, X. Lu, et al., Mater. Today 63 (2023) 339–359.
[24] S. Siahrostami, A. Verdaguer-Casadevall, M. Karamad, et al., Nat. Mater. 12 (2013) 1137–1143.
[25] X. Zhao, H. Yang, J. Xu, T. Cheng, Y. Li, ACS Mater. Lett. 3 (2021) 996–1002.
[26] Z. Lu, G. Chen, S. Siahrostami, et al., Nat. Catal. 1 (2018) 156–162.
[27] L. Li, C. Tang, Y. Zheng, et al., Adv. Energy Mater. 10 (2020) 2000789.
[28] K. Dong, J. Liang, Y. Wang, et al., ACS Catal. 12 (2022) 6092–6099.
[29] M. Wang, X. Dong, Z. Meng, et al., Angew. Chem. Int. Ed. 60 (2021) 11190–11195.
[30] S. Ding, B. Xia, M. Li, et al., Energy Environ. Sci. 16 (2023) 3363–3372.
[31] Y. Yao, H. Wang, K. Dong, et al., J. Mater. Chem. A 11 (2023) 22154–22160.
[32] L. Zhang, J. Liang, L. Yue, et al., Nano Res. 15 (2022) 304–309.
[33] X.L. Zhang, X. Su, Y.R. Zheng, et al., Angew. Chem. Int. Ed. 60 (2021) 26922.
[34] F. Xia, B. Li, Y. Liu, et al., Adv. Funct. Mater. 31 (2021) 2104716.
[35] F. Ma, S. Wang, X. Liang, et al., Appl. Catal. B 279 (2020) 119371.
[36] S. Xu, Y. Gao, T. Liang, L. Zhang, B. Wang, Chin. Chem. Lett. 33 (2022) 5152–5157.
[37] J.Y. Zhang, C. Xia, H.F. Wang, C. Tang, J. Energy Chem. 67 (2022) 432–450.
[38] J. Liu, Z. Gong, M. Yan, et al., Small 18 (2022) 2103824.
[39] Y. Pang, H. Xie, Y. Sun, M.M. Titirici, G.L. Chai, J. Mater. Chem. A 8 (2020) 24996–25016.
[40] Q. Yang, W. Xu, S. Gong, et al., Nat. Commun. 11 (2020) 5478.
[41] Z. Chen, J. Wu, Z. Chen, et al., Angew. Chem. Int. Ed. 61 (2022) e202200086.
[42] W. Liu, J. Feng, R. Yin, et al., Chem. Eng. J. 430 (2022) 132990.
[43] X. Zhang, Y. Xia, C. Xia, H. Wang, Trends Chem. 2 (2020) 942–953.
[44] S. Yang, A. Verdaguer-Casadevall, L. Arnarson, et al., ACS Catal. 8 (2018) 4064–4081.
[45] B. Sabri Rawah, M. Albloushi, W. Li, Chem. Eng. J. 466 (2023) 143282.
[46] A. Huang, R.S. Delima, Y. Kim, et al., J. Am. Chem. Soc. 144 (2022) 14548–14554.
[47] M. Li, H. Lan, X. An, et al., Appl. Catal. B 339 (2023) 123125.
[48] M.A. Modestino, D.Fernandez Rivas, S.M.H. Hashemi, J.G.E. Gardeniers, D. Psaltis, Energy Environ. Sci. 9 (2016) 3381–3391.
[49] Z. Wei, H. Xu, Z. Lei, et al., Chin. Chem. Lett. 33 (2022) 920–925.
[50] H. Sheng, A.N. Janes, R.D. Ross, et al., Nat. Catal. 5 (2022) 716–725.
[51] J.H. Kim, D. Shin, J. Lee, et al., ACS Nano 14 (2020) 1990–2001.
[52] X. Zhao, Y. Liu, J. Am. Chem. Soc. 143 (2021) 9423–9428.
[53] K. Liu, P. Chen, Z. Sun, et al., Nano Res. 16 (2023) 10724–10741.
[54] Y. Cheng, H. Wang, H. Song, et al., Nano Res. Energy 2 (2023) e9120082.
[55] X. Guo, S. Lin, J. Gu, et al., ACS Catal. 9 (2019) 11042–11054.
[56] A. Kulkarni, S. Siahrostami, A. Patel, J.K. Nørskov, Chem. Rev. 118 (2018) 2302–2312.
[57] V. Viswanathan, H.A. Hansen, J. Rossmeisl, J.K. Nørskov, J. Phys. Chem. Lett. 3 (2012) 2948–2951.
[58] X. Wang, Z. Li, Y. Qu, et al., Chem 5 (2019) 1486–1511.
[59] X. Zhang, C. Wang, K. Chen, et al., Adv. Mater. 35 (2023) 2211512.
[60] S.J. Freakley, Q. He, J.H. Harrhy, et al., Science 351 (2016) 965–968.
[61] Q. Chang, P. Zhang, A.H.B. Mostaghimi, et al., Nat. Commun. 11 (2020) 2178.
[62] Z. Yu, S. Lv, Q. Yao, et al., Adv. Mater. 35 (2023) 2208101.
[63] M. Song, W. Liu, J. Zhang, et al., Adv. Funct. Mater. 33 (2023) 2212087.

[64] Y. Sun, L. Silvioli, N.R. Sahraie, et al., J. Am. Chem. Soc. 141 (2019) 12372–12381.
[65] Q. Zhang, L. Zheng, F. Gu, et al., Nano Energy 116 (2023) 108798.
[66] Z. Zhuang, A. Huang, X. Tan, et al., Joule 7 (2023) 1003–1015.
[67] L. Wang, J. Wu, S. Wang, et al., Nano Res. 17 (2024) 3261–3301.
[68] T. Gan, D. Wang, Nano Res. 17 (2024) 18–38.
[69] C. Tang, L. Chen, H. Li, et al., J. Am. Chem. Soc. 143 (2021) 7819–7827.
[70] E. Jung, H. Shin, B.H. Lee, et al., Nat. Mater. 19 (2020) 436–442.
[71] H. Shen, N. Qiu, L. Yang, et al., Small 18 (2022) 2200730.
[72] L. Jing, Q. Tian, P. Su, et al., J. Mater. Chem. A 10 (2022) 4068–4075.
[73] C. Liu, Z. Yu, F. She, et al., Energy Environ. Sci. 16 (2023) 446–459.
[74] Y.X. Du, Q. Yang, W.T. Lu, et al., Adv. Funct. Mater. 33 (2023) 2300895.
[75] J. Du, G. Han, W. Zhang, et al., Nat. Commun. 14 (2023) 4766.
[76] Y. Wang, R. Shi, L. Shang, et al., Angew. Chem. Int. Ed. 59 (2020) 13057–13062.
[77] C. Tang, Y. Jiao, B. Shi, et al., Angew. Chem. Int. Ed. 59 (2020) 9171–9176.
[78] E. Berl, Trans. Electrochem. Soc. 76 (1939) 359.
[79] Q. Wang, L. Ren, J. Zhang, et al., Adv. Energy Mater. 13 (2023) 2301543.
[80] G. Wei, Y. Li, X. Liu, et al., Angew. Chem. Int. Ed. 62 (2023) e202313914.
[81] J. Huang, C. Fu, J. Chen, et al., CCS Chem. 4 (2022) 566–583.
[82] K. Dong, J. Liang, Y. Wang, et al., Angew. Chem. Int. Ed. 60 (2021) 10583–10587.
[83] Z. Bao, J. Zhao, S. Zhang, et al., Nano Res. 16 (2023) 9050–9058.
[84] H. Jiang, C. Zhang, Z. Wang, et al., Appl. Catal. A 661 (2023) 119242.
[85] Q. Yuan, J. Zhao, D.H. Mok, et al., Nano Lett. 22 (2021) 1257–1264.
[86] J. Wu, M. Hou, Z. Chen, et al., Adv. Mater. 34 (2022) 2202995.
[87] Y. Pang, K. Wang, H. Xie, et al., ACS Catal. 10 (2020) 7434–7442.
[88] G.L. Chai, Z. Hou, T. Ikeda, K. Terakura, J. Phys. Chem. C 121 (2017) 14524–14533.
[89] N. Ramaswamy, S. Mukerjee, J. Phys. Chem. C 115 (2011) 18015–18026.
[90] M. Ko, Y. Kim, J. Woo, et al., Nat. Catal. 5 (2022) 37–44.
[91] C. Xia, Y. Xia, P. Zhu, L. Fan, H. Wang, Science 366 (2019) 226–231.
[92] H. Li, P. Wen, D.S. Itanze, et al., Nat. Commun. 11 (2020) 3928.
[93] H. Sheng, R.D. Ross, J.R. Schmidt, S. Jin, ACS Energy Lett. 8 (2023) 196–212.
[94] L. Sun, X. Jin, T. Su, A.C. Fisher, X. Wang, Adv. Mater. 36 (2024) 2306336.
[95] Y. Wang, H. Yang, Z. Liu, et al., J. Energy Chem. 87 (2023) 247–255.
[96] Z. Su, Q. Huang, Q. Guo, et al., Nano Res. Energy 2 (2023) e9120078.
[97] Z. Che, X. Lu, B. Cai, et al., Nano Res. 15 (2022) 1269–1275.
[98] L.P. Yuan, T. Tang, J.S. Hu, L.J. Wan, Acc. Mater. Res. 2 (2021) 907–919.
[99] S. Geng, Y. Ji, S. Yang, et al., Adv. Funct. Mater. 33 (2023) 2300636.
[100] Y. Zhang, M. Wang, W. Zhu, et al., Angew. Chem. Int. Ed. 62 (2023) e202218924.
[101] E.L. Gyenge, C.W. Oloman, J. Appl. Electrochem. 31 (2001) 233–243.
[102] X. Zhang, X. Zhao, P. Zhu, et al., Nat. Commun. 13 (2022) 2880.
[103] E. Jung, H. Shin, W. Hooch Antink, Y.E. Sung, T. Hyeon, ACS Energy Lett. 5 (2020) 1881–1892.
[104] Y. Jiang, P. Ni, C. Chen, et al., Adv. Energy Mater. 8 (2018) 1801909.
[105] J. An, N. Li, Y. Wu, et al., Environ. Sci. Technol. 54 (2020) 10916–10925.
[106] R.M. Sellers, Analyst 105 (1980) 950–954.
[107] J. Xie, J. Jing, J. Gu, et al., J. Environ. Chem. Eng. 10 (2022) 107882.
[108] Z. Xing, K. Shi, Z.S. Parsons, X. Feng, ACS Catal. 13 (2023) 2780–2789.
[109] Y. Wang, R. Shi, L. Shang, et al., Nano Energy 96 (2022) 107046.
[110] E. Zhang, L. Tao, J. An, et al., Angew. Chem. Int. Ed. 61 (2022) e202117347.
[111] W. Zhou, X. Meng, L. Rajic, et al., Electrochem. Commun. 96 (2018) 37–41.
[112] J. An, Y. Feng, N. Wang, et al., J. Hazard. Mater. 428 (2022) 128185.
[113] H. Zhang, S. Wu, X. Huang, et al., Chem. Eng. J. 428 (2022) 131534.
[114] Z. Chen, S. Chen, S. Siahrostami, et al., React. Chem. Eng. 2 (2017) 239–245.
[115] C. Xia, S. Back, S. Ringe, et al., Nat. Catal. 3 (2020) 125–134.
[116] B. Xia, Q. Huang, H. Wang, et al., ACS Appl. Mater. Interfaces 15 (2023) 32416–32424.
[117] Z. Lin, Q. Zhang, J. Pan, et al., Energy Environ. Sci. 15 (2022) 1172–1182.
[118] E. Ruiz-López, E. Amores, A. Raquel de la Osa, F. Dorado, A. de Lucas-Consuegra, Chem. Eng. J. 379 (2020) 122289.
[119] S.M.H. Hashemi, P. Karnakov, P. Hadikhani, et al., Energy Environ. Sci. 12 (2019) 1592–1604.
[120] P. Farinazzo Bergamo Dias Martins, I. Plazl, D. Strmcnik, B. Genorio, Curr. Opin. Electrochem. 38 (2023) 101223.
[121] H. Sheng, A.N. Janes, R.D. Ross, et al., Energy Environ. Sci. 13 (2020) 4189–4203.
[122] H. Yin, Y. Dou, S. Chen, et al., Adv. Mater. 32 (2020) 1904870.
[123] R.J. Lewis, K. Ueura, X. Liu, et al., ACS Catal. 13 (2023) 1934–1945.
[124] S. Wu, H. Zhang, X. Huang, Z. Wei, Chem. Commun. 58 (2022) 8942–8945.